Reynolds stress budgets in Couette and boundary layer flows

By Jukka Komminaho and Martin Skote

Dept. of Mechanics, KTH, SE-100 44, Stockholm, Sweden

Reynolds stress budgets for both Couette and boundary layer flows are evaluated and presented. Data are taken from direct numerical simulations of rotating and non-rotating plane turbulent Couette flow and turbulent boundary layer with and without adverse pressure gradient. Comparison of the total shear stress for the two flows suggests that the Couette case may be regarded as the high Reynolds number limit for the boundary layer flow close to the wall. The direction of rotation is chosen so that it has a stabilizing effect, whereas the adverse pressure gradient is destabilizing. The pressure strain-rate tensor is in the Couette flow case presented for a split into slow, rapid and Stokes terms.

1. Introduction

The development of cheap, powerful, computers has lead to wide use of CFD codes for the prediction of turbulent flows. These codes almost always use turbulence models to try to capture the characteristics of the turbulent flow, and the prediction is no better than the weakest link in computational chain. Often the weakest link is the turbulence model. But to develop better turbulence models one must have data to compare them against. In the early days of turbulence modelling one had to rely on indirect methods to test the various closure models. Experimental difficulties in measuring pressure and velocity with sufficient resolution did not make direct comparisons possible.

With the development of high-speed supercomputers, and new algorithms, Orszag (1969, 1970); Kreiss & Oliger (1972); Basdevant (1983), it became possible to simulate turbulent flows directly without resorting to large eddy simulations or turbulence models. Now it became possible to evaluate any desirable quantity and use them to test turbulence models. The channel flow simulation by Kim *et al.* (1987) was the first fully resolved simulation of a pressure-driven channel flow, and the database from the simulation has been used extensively to evaluate various turbulence models, Mansour *et al.* (1988).

There are few experimental studies of Couette flow with reports of turbulence statistics. In the study of Couette flow at a Reynolds number of 1300, Bech *et al.* (1995), report both second and higher order statistics from both

experiments and simulations. The agreement between the experiments and the simulation is good for the statistics, but their simulations do not fully capture the very large scale structures of the experiments. This is e.g. seen from the two-point correlations which are lower in the simulation than in the experiment. In Bech & Andersson (1994) they used three different sizes of computational domain and observed large structures in one box, but not in the other two. The reason behind this is unclear.

In Bech (1995) they present Reynolds stress budgets from the simulation in Bech *et al.* (1995), and they look very similar to the ones presented here, despite the higher Reynolds number in their simulation.

In the present paper the budget data for the Reynolds stresses in the Couette flow case are evaluated from the flow fields of the plane Couette flow simulation by Komminaho *et al.* (1996).

Data are also presented from three different turbulent boundary layers. One is a zero pressure gradient (ZPG) boundary layer, and two are boundary layers subject to an adverse pressure gradient (APG). Data from the ZPG boundary layer have not previously been presented. The simulation with a moderate APG (APG1) has been analyzed in Skote *et al.* (1998), while the strong APG case (APG2) has been presented in Skote & Henningson (2000).

The ZPG turbulent boundary layer flow has been studied in a large number of investigations, see e.g. the assessment of data by Fernholz & Finley (1996). Turbulent statistics close to the wall were obtained through DNS by Spalart (1988), and were confirmed later in the experiment of a low Reynolds number ZPG turbulent boundary layer by Ching *et al.* (1995). Various Reynolds stress budgets from DNS of both ZPG and APG boundary layers were presented by Na & Moin (1996). Near-wall limit values of an APG boundary layer were also investigated in the DNS of Spalart & Watmuff (1993) and in the experiment of Nagano *et al.* (1992).

The results from the simulations of Komminaho *et al.* (1996), Skote *et al.* (1998) and Skote & Henningson (2000) are documented here for future use in turbulence model development, in particular for near-wall modelling. The present plane Couette flow data are well suited for this purpose since the condition of a constant total shear is, unlike the situation in the boundary layer, fulfilled for all Reynolds numbers. The boundary layer data can be used for the development of low Reynolds number turbulence models.

2. Data analysis

One can write the Navier–Stokes and continuity equations in a rotating reference frame as,

$$\frac{\partial u_i'}{\partial t} + \frac{\partial}{\partial x_j}(u_i' u_j') = -\frac{1}{\rho}\frac{\partial p'}{\partial x_i} + \nu \frac{\partial^2 u_i'}{\partial x_j \partial x_j} + 2\epsilon_{ijk} u_j' \Omega_k \tag{1a}$$

$$\frac{\partial u_i'}{\partial x_i} = 0. \tag{1b}$$

The effect of the system rotation can be seen as a volume force in the fluid, also known as the Coriolis force and the centrifugal force. The Coriolis force is the last term in the momentum equation, and the centrifugal force has been included in the pressure.

Divide the flow into a mean and a fluctuating part, $u' = U + u$, where the mean part is defined as an ensemble average over N different times, and also an average over the homogeneous directions (x and z in the Couette flow and z in the boundary layer)

$$\overline{u'} \equiv U(y,t) = \frac{1}{NL_xL_z} \sum_{i=1}^{N} \int_0^{L_x} \int_0^{L_z} u'(x,y,z,t) \mathrm{d}x \mathrm{d}z. \tag{2}$$

The Reynolds equation for the mean flow is now obtained as

$$\frac{\partial U_i}{\partial t} + \frac{\partial}{\partial x_j}(U_iU_j) = -\frac{1}{\rho}\frac{\partial P}{\partial x_i} + \nu \frac{\partial^2 U_i}{\partial x_j \partial x_j} - \frac{\partial}{\partial x_j} R_{ij} + \epsilon_{ijk} U_j \Omega_k \tag{3}$$

where $R_{ij} = \overline{u_iu_j}$ is the velocity correlation tensor, and will here be referred to as the 'Reynolds stress tensor'.

2.1. *Couette data*

Plane Couette flow is the flow between two parallel planes, moving in opposite directions with velocity $\pm U_w$ in the x-direction, at a distance $2h$. The wall-normal direction is denoted y. The system rotation Ω applied in the present work is around the z axis.

The various statistical quantities have been evaluated and averaged from 12 different velocity fields, and the average was taken in both x and z direction. The time between the samples was $T = 40$, and they are statistically independent for all but the very largest scales, see Komminaho *et al.* (1996) where the time scale for the integral length scale (Λ_{uux} defined as $\int R_{uu}(\Delta x)\mathrm{d}x$, R_{uu} being the two-point velocity correlation) was found to be more than 50.

2.2. *Boundary layer data*

The statistics have been produced in the same manner as in the Couette case, except for the important difference that the flow is not homogeneous in the streamwise (x) direction. The boundary layer is growing and developing in the $x-$direction due to the increasing Reynolds number. Thus, the statistics are unique for each streamwise position. However, here we are only dealing with the near-wall statistics, which in the viscous scaling should be invariant under the Reynolds number. But in the low Reynolds number flows simulated with DNS, there is a small influence of the increasing Reynolds number. This effect is confined to the part very close to the wall ($y^+ < 3$). In the ZPG simulation e.g., the boundary layer undergoes a doubling of the Reynolds number, but the budgets fall on top of each other for different streamwise positions, except for the small increase of the values at the wall. The statistics are therefore shown for one streamwise position in all three cases.

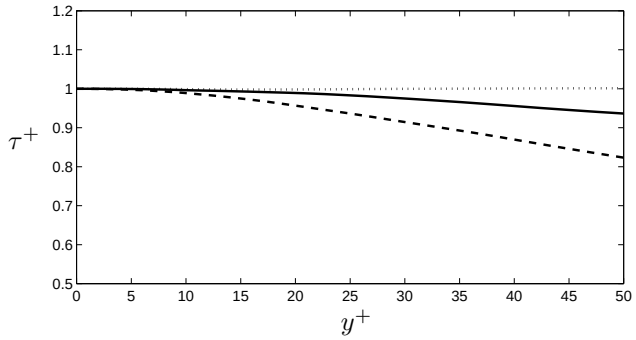

FIGURE 1. Total shear stress. Couette ($\cdots$). Boundary layer: (- -) $Re_{\delta_*} = 539$, (—) $Re_{\delta_*} = 920$.

The simulations APG1 and APG2 were performed with a pressure distribution leading to a self-similar boundary layer at high Reynolds numbers. The pressure gradient parameter β,

$$\beta \equiv \frac{\delta_*}{\tau_w} \frac{\mathrm{d}P}{\mathrm{d}x}, \tag{4}$$

defines the APG in these two simulations.

The Reynolds number at the position where the budgets have been evaluated is shown in table 1, together with the local value of the friction velocity, freestream velocity and pressure gradient parameter.

Case	Re_{δ_*}	Re_Θ	u_τ	U	β
ZPG	920	606	0.048	1.0	0.0
APG1	1064	655	0.036	0.76	0.65
APG2	2573	1309	0.020	0.60	5.0

TABLE 1. Reynolds number, friction velocity, freestream velocity and pressure gradient at the streamwise position where the Reynolds stress budgets have been evaluated.

Another effect of the Reynolds number is the increasing length of the region with constant shear stress (τ^+). This is illustrated in figure 1, which shows the total shear stress at two Reynolds numbers for the ZPG case, as well as for Couette flow. From figure 1 it is clear that the total shear stress for the boundary layer becomes more constant when the Reynolds number is increased. Since τ^+ is constant for the Couette flow, it might be argued that this flow approximates a high Reynolds number boundary layer close to the wall.

2.3. *Reynolds stress budget*

The transport equations for the Reynolds stress tensor are obtained by multiplying (1a) (after subtracting the mean equation 3) with u_j, adding the corresponding equation with switched indices i, j and ensemble averaging. The resulting equations read

$$\frac{\mathrm{D}R_{ij}}{\mathrm{D}t} \equiv \left(\frac{\partial}{\partial t} + U_j \frac{\partial}{\partial x_j}\right) R_{ij} = \mathcal{P}_{ij} - \varepsilon_{ij} + \Pi_{ij} + G_{ij} + D_{ij} + T_{ij} + C_{ij} \quad (5)$$

where

$$\mathcal{P}_{ij} \equiv -\overline{u_i u_k}\frac{\partial U_j}{\partial x_k} - \overline{u_j u_k}\frac{\partial U_i}{\partial x_k}, \quad (6a)$$

$$\varepsilon_{ij} \equiv 2\nu\overline{u_{i,k}u_{j,k}}, \quad (6b)$$

$$D_{ij} \equiv \frac{\partial}{\partial x_k}\left(\nu R_{ij,k}\right), \quad (6c)$$

$$\Pi_{ij} \equiv \frac{1}{\rho}\left(\overline{p\frac{\partial u_i}{\partial x_j} + p\frac{\partial u_j}{\partial x_i}}\right), \quad (6d)$$

$$G_{ij} \equiv -\frac{\partial}{\partial x_k}\left(\frac{1}{\rho}\overline{u_j p}\delta_{ik} + \frac{1}{\rho}\overline{u_i p}\delta_{jk}\right), \quad (6e)$$

$$T_{ij} \equiv -\frac{\partial}{\partial x_k}\overline{u_i u_j u_k}, \quad (6f)$$

$$C_{ij} \equiv -2\Omega_k\left(R_{lj}\epsilon_{ikl} + R_{il}\epsilon_{jkl}\right). \quad (6g)$$

Here $\mathcal{P}_{ij}$ is the production due to mean field gradients, whose trace ($\mathcal{P}_{ii}$) represents twice the production of turbulent energy, the transfer of energy from the mean flow to the turbulent fluctuations.

ε_{ij} is the dissipation rate tensor, and D_{ij} is the diffusion tensor. They both represent viscous effects, but whereas D_{ij} is a molecular diffusion term acting to even out the turbulent stresses by spatial redistribution, ε_{ij} act as a destruction term of turbulent energy (and stresses).

Π_{ij} is the pressure-strain rate correlation tensor, which is traceless and represents inter-component transfer between Reynolds stress terms. G_{ij} is the divergence of the pressure-velocity correlation, and represents transport driven by pressure fluctuations. This split in the above two terms is not unique, there are several different ways in which one may separate the pressure-velocity term when deriving the RST equations, but as the investigation in Groth (1991) shows the above separation seems to make most physical sense.

T_{ij} is the divergence of the triple correlation tensor, acting as a spatial redistribution term.

C_{ij} is the traceless Coriolis tensor, which acts as a redistributive term among the stress components.

The transport equation for the kinetic energy, $K \equiv \frac{1}{2}\mathcal{P}_{ii}$ is

$$\frac{\mathrm{D}K}{\mathrm{D}t} = \mathcal{P} - \varepsilon + \mathcal{D}, \quad (7)$$

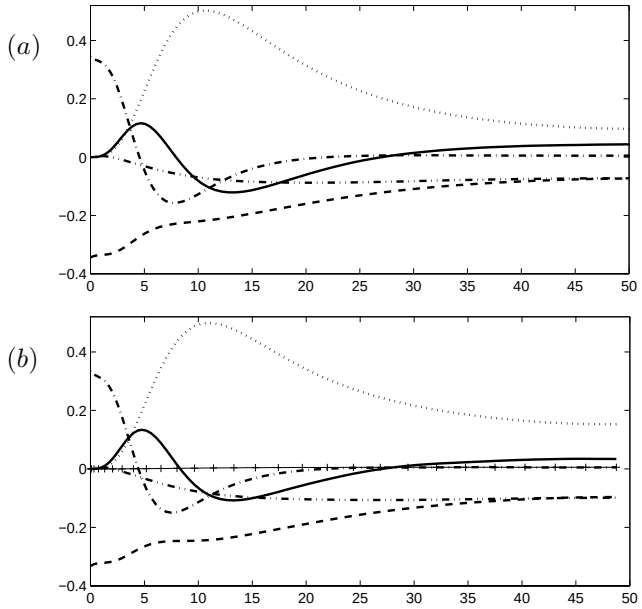

FIGURE 2. Terms in the Couette flow R_{11}-budget for (a) the non-rotating case and (b) the rotating case, $\Omega = -0.005$. The different terms are: ($\cdots$) $\mathcal{P}_{11}$, (- -) $-\varepsilon_{11}$, (- · -) D_{11}, (- · · -) Π_{11}, (—) T_{11}, (+) C_{11}.

where $\mathcal{P} = \frac{1}{2}\mathcal{P}_{ii}$ is the turbulent energy production, $\varepsilon = \frac{1}{2}\varepsilon_{ii}$ is the viscous dissipation, and $\mathcal{D} = \frac{1}{2}\left(T_{ii} + G_{ii} + D_{ii}\right)$ is the sum of the molecular and turbulent diffusion of K. This term acts as a spatial redistribution of K.

In a fully developed plane Couette flow, the flow is homogeneous in the x and z directions, and the relevant non-zero stresses are R_{11}, R_{12}, R_{22} and R_{33}. Figures 2–9 show the terms in the budget of these stresses, as functions of the wall-normal distance $y^+ = yu_\tau/\nu$, where $u_\tau = \sqrt{\tau_w/\rho}$ is the friction velocity. Note that in the non-rotating case the Coriolis term, C_{ij}, is zero. All quantities are shown in $^+$-units, non-dimensionalized with u_τ^4/ν. The simulation flow fields represent a plane Couette flow at a Reynolds number $Re_\tau = u_\tau h/\nu = 52$ ($Re_\tau = 48$ for the rotating case) based on friction velocity u_τ and channel half-height h. This corresponds to a Reynolds number 750 based on wall-velocity and h. Despite this very low Reynolds number it is twice that of the transition Reynolds number of 360, Lundbladh & Johansson (1991); Tillmark & Alfredsson (1992); Komminaho *et al.* (1997). For the rotating case the rotation is as low as $\Omega = -0.005$, corresponding to a Rossby number of 200.

The budgets for the Reynolds stresses in the ZPG case are essentially the same as in Spalart (1988). The moderate APG case, APG1, show very similar profiles in the Reynolds stress budgets as the APG simulation of Na & Moin

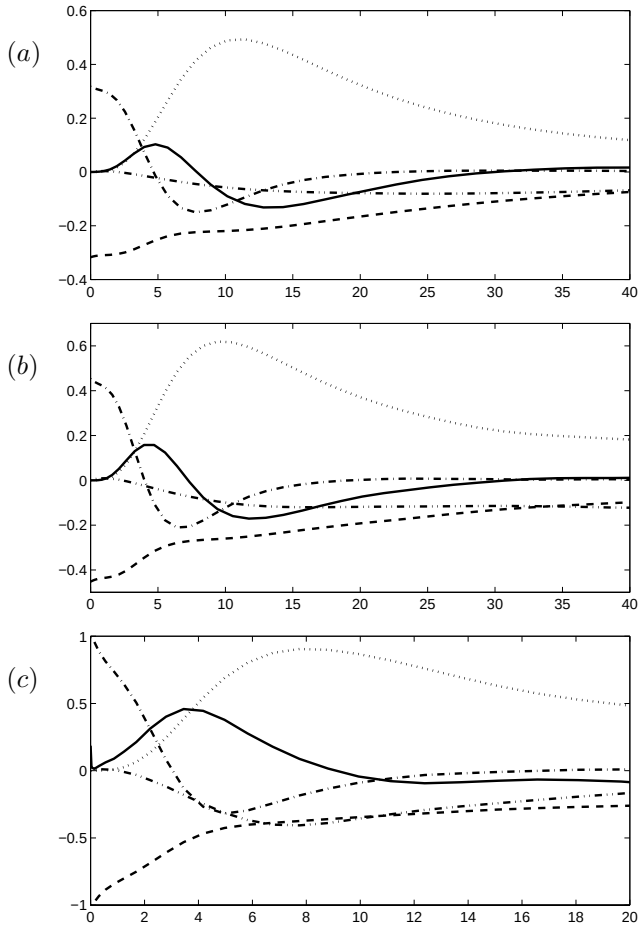

FIGURE 3. Terms in the R_{11}-budget for boundary layer flow (*a*) ZPG. (*b*) APG1. (*c*) APG2. The different terms are: $(\cdots)$ $\mathcal{P}_{11}$, (- -) $-\varepsilon_{11}$, (- · -) D_{11}, (- · · -) Π_{11}, (—) T_{11}.

(1996). The effects of the APG will be stronger in the APG2 case, which has a skin friction approximately 60 % of that in APG1. In this work, in contrast to the budgets in Spalart (1988) and Na & Moin (1996), the pressure term is divided into pressure-strain and pressure-velocity diffusion, for comparison with the Couette data.

In figures 2 to 9 the budgets for the Reynolds stresses are shown. The figures include both non-rotating and rotating Couette flow as well as all three boundary layer cases and the profiles from the ZPG case can be compared with the Couette case with zero rotation.

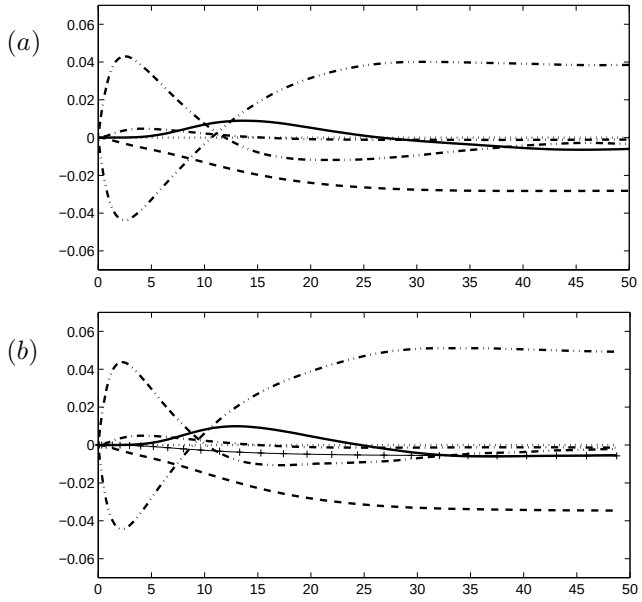

FIGURE 4. Terms in the Couette flow R_{22}-budget for (a) the non-rotating case and (b) the rotating case, $\Omega = -0.005$. The different terms are: (- -) $-\varepsilon_{22}$, (- · -) D_{22}, (- · · -) Π_{22}, (- - · ·) G_{22}, (—) T_{22}, (+) C_{22}.

2.3.1. *Longitudal Reynolds stress*

One may note that the maximum of the production term $\mathcal{P}_{11}$ is 0.5. This is easily obtained by integrating the stream-wise momentum equation once, and multiplying with $\frac{dU^+}{dy^+}$. The advection term is zero in the Couette flow case negligible in the near-wall region for boundary layers. By neglecting the advection term and assuming wall similarity, we obtain the following relation for the turbulence production:

$$\mathcal{P}_{11} \equiv -2\frac{\overline{uv}}{u_\tau^2}\frac{\mathrm{d}U^+}{\mathrm{d}y^+} = 2\frac{\mathrm{d}U^+}{\mathrm{d}y^+}\left(1 - \frac{\mathrm{d}U^+}{\mathrm{d}y^+} + \frac{\nu}{\rho u_\tau^3}\frac{\mathrm{d}P}{\mathrm{d}x}y^+\right), \tag{8}$$

where the pressure gradient term is non-zero only in the adverse pressure gradient (APG) cases. The last term within the parenthesis can be rewritten as $\beta y^+/\delta_*^+$. From the above relation it follows that the maximum of $\mathcal{P}_{11}$ is 0.5 occurring at a position where $\mathrm{d}U^+/\mathrm{d}y^+ = 0.5$ for Couette flow and ZPG boundary layer. This holds irrespective of the value of the Reynolds number and the system rotation and was shown to accurately describe also the low-Reynolds number plane Couette flow simulation of Komminaho *et al.* (1997) where the Reynolds number was as low as 375.

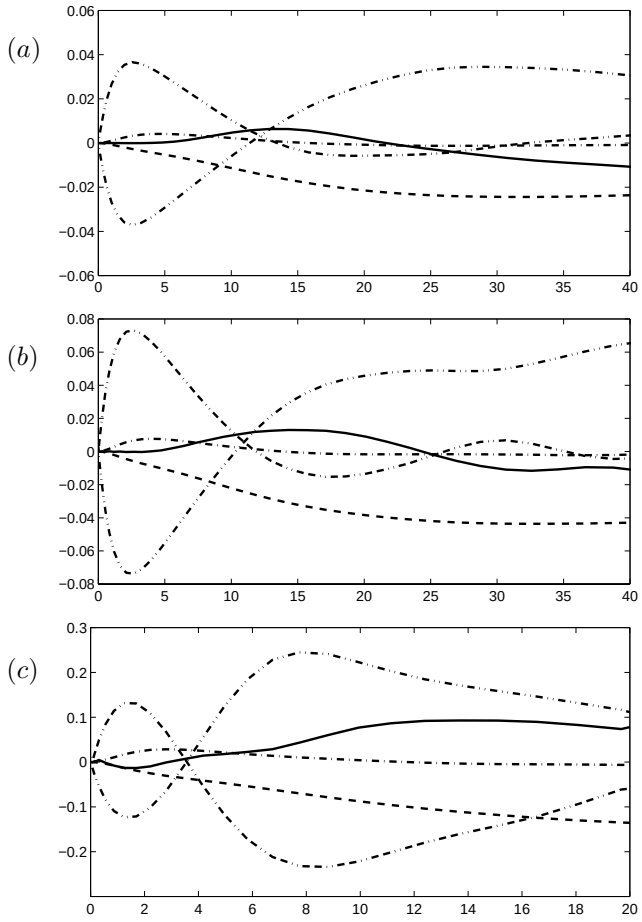

FIGURE 5. Terms in the R_{22}-budget for boundary layer flow (*a*) ZPG. (*b*) APG1. (*c*) APG2. The different terms are: (- -) $-\varepsilon_{22}$, (- · -) D_{22}, (- · · -) Π_{22}, (- - · ·) G_{22}, (—) T_{22}.

The overall character of the different terms in the Reynolds stress budget for R_{ij} is the same as for the channel flow in Mansour *et al.* (1988). Figure 2 shows that the production term $\mathcal{P}_{11}$ is the dominant positive term in the range $y^+ > 5$, and has a maximum of 0.5 in the buffer region, at $y^+ = 11$, falling to 0.10 in the centre of the channel. The location of the peak production can be found to be $y^+ \approx 11$ also in channel and pipe flow, Sahay & Sreenivasan (1999). The non-zero production in the central region is a consequence of the non-zero mean shear in this region.

Π_{11} is negative throughout the channel, thereby transferring energy from R_{11} to R_{22} and R_{33}.

Despite the very low rotation rate for the Couette flow case the effects on some terms in the budgets are significant, away from the wall. The production $\mathcal{P}_{11}$ is about 60% larger in the centre of the channel for the rotating case. The dissipation ε_{11} and the pressure-strain-rate Π_{11} are both 30% larger for the rotating case, whereas the redistributive term T_{11} is about 20% smaller. Near the walls the non-rotating and rotating cases are very similar, as can be expected since the maximum production is 0.5 in both cases.

In figure 3a the budget for the longitudal Reynolds stress is shown for the ZPG case. The maximum of the production term $\mathcal{P}_{11}$ is 0.5 as in the Couette case. The other terms in the budget for R_{11} corresponds very closely to those in the Couette case. The adverse pressure gradient increases the production $\mathcal{P}_{11}$ as seen in figures 3b and c. For APG1 it is 0.6 and APG2 0.9. The increase of the maximum is not explained by the contribution from the streamwise velocity gradient since that part of the production term is negligible close to the wall.

The increased value of $\mathcal{P}_{11}$ is thus explained from the contribution from the pressure gradient in equation (8). For the case APG2 we have a δ_*^+ of 86 so that the last term within the parenthesis in equation (8) $\beta y^+/\delta_*^+$ is about 0.58 at $y^+ = 10$, i.e. near the maximum in production. It can, hence, be seen to be of the order one influence. Since $\beta y^+/\delta_*^+ = \beta y^+ \frac{U_\infty}{u_\tau}/Re_{\delta_*}$ we can see that the effect of the pressure gradient term decreases with increasing Reynolds number.

The position of the maximum is shifted towards the wall, most notably in the APG2 case (figure 3c).

Also the rest of terms show more extreme values in the APG cases, even though the shape of the profiles remain roughly the same. The enhanced values in the near-wall region are partly due to the decrease in the friction velocity (which all the terms in the budget are scaled with). The lower value of u_τ is a consequence of the adverse pressure gradient. One might argue that u_τ is not the correct scaling in an APG flow, since the total shear stress is not constant in this scaling. Alternative scalings, including a velocity scale dependent on the wall normal distance that produce a constant shear stress, are discussed in Skote & Henningson (1999) and Skote & Henningson (2000).

2.3.2. *Normal Reynolds stress*

In figure 4 the budget for R_{22} in the Couette flow case is shown. Π_{22} is negative close to the wall, and positive towards the centre. Thus it transfers energy from the wall-normal components to the horizontal components near the wall. This reversal of the sign was attributed to the splatting effect in the LES study of turbulent channel flow by Moin & Kim (1982) (see also Hunt & Graham 1978). In the turbulence modelling context this effect is normally referred to as the wall-reflection contribution to the pressure strain. The attempts to model this (see Gibson & Launder 1978) typically assumes a variation on a length-scale of the order of the macro-scale. The present results and those of Aronson *et al.* (1997) and Perot & Moin (1995) however show that the effect is confined to a thin region near the wall. In some recent model development (see e.g. Sjögren

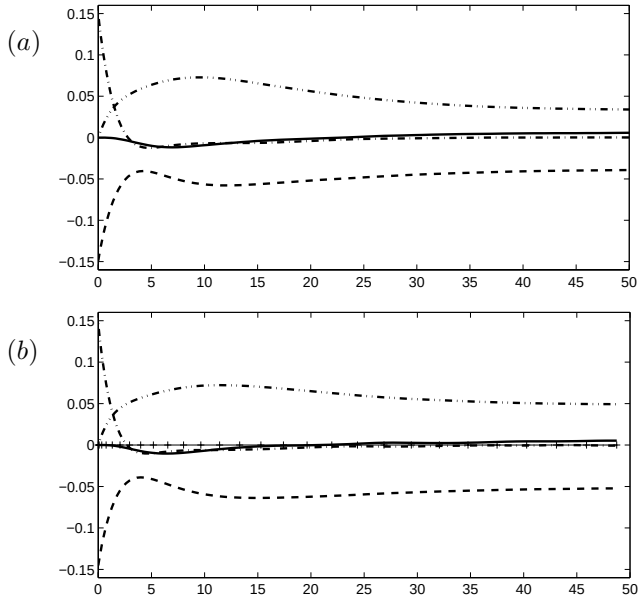

FIGURE 6. Terms in the Couette flow R_{33}-budget for (a) the non-rotating case and (b) the rotating case, $\Omega = -0.005$. The different terms are: (- -) $-\varepsilon_{33}$, (- · -) D_{33}, (- · · -) Π_{33}, (—) T_{33}, (+) C_{33}.

& Johansson 2000) this effect is only indirectly accounted for through realizable models.

The same trend regarding the dissipation and the pressure-strain rate can also be seen in figures 4 and 6 for R_{22} and R_{33} budgets.

In figure 5a the budget for R_{22} in the ZPG case is shown. All the terms show slightly lower values than in the Couette case, while the shapes of the profiles are similar. As the pressure gradient increases, all the terms become larger, as seen from figures 5b and c. A peak in the pressure-strain term has developed in the APG2 case at the position $y^+ = 8$, and exceeds the maximum value of the pressure diffusion. The formation of a peak is not observed in the ZPG and APG1 cases, where a plateau is developed in the pressure-strain, and the value is lower than the pressure-velocity gradient.

2.3.3. *Spanwise Reynolds stress*

In the ZPG budget for the spanwise Reynolds stress, shown in figure 7a, the values of the different terms are, as in the R_{22} budget, lower than in the Couette flow. The shapes of the profiles are similar to those in the Couette case. The pressure gradient enhances the values, but nothing else seems to be affected

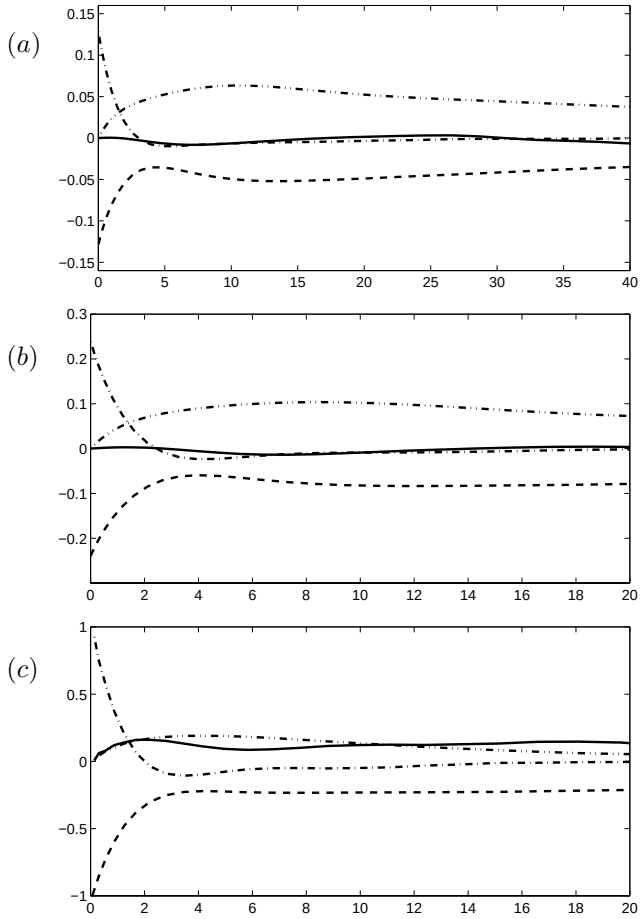

FIGURE 7. Terms in the R_{33}-budget for boundary layer flow (*a*) ZPG. (*b*) APG1. (*c*) APG2. The different terms are: (- -) $-\varepsilon_{33}$, (- · -) D_{33}, (- · · -) Π_{33}, (—) T_{33}.

in the APG1 case. In APG2 however, the turbulent transport is of the same magnitude as the pressure-strain.

2.3.4. *Reynolds shear stress*

The budget for the Reynolds shear stress in Couette flow is presented in figure 8. The pressure strain (Π_{12}) and pressure diffusion (G_{12}) balance each other at the wall. This is also the case in Mansour *et al.* (1988). The value of Π_{12} at the wall in Couette flow is more than twice the value found in the channel flow simulation Mansour *et al.*, and also for ZPG flow it is higher.

The budget for the Reynolds shear stress in boundary layer flow is presented in figure 9. The profiles are approximately the same as in the Couette case,

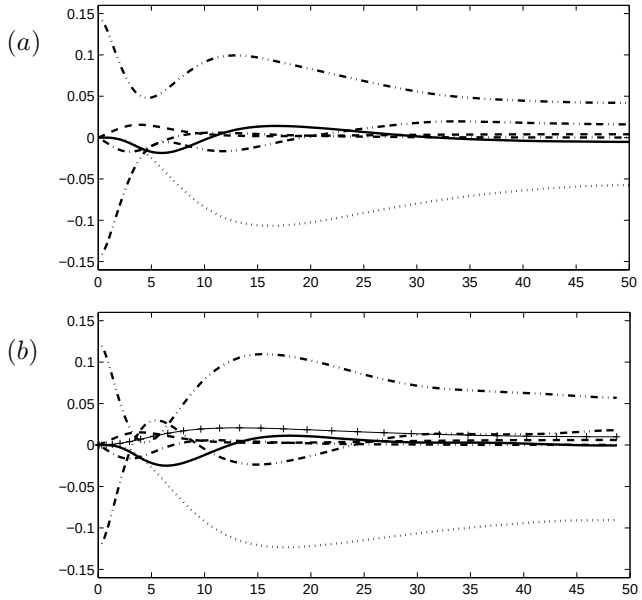

FIGURE 8. Terms in the Couette flow R_{12}-budget for (a) the non-rotating case and (b) the rotating case, $\Omega = -0.005$. The different terms are: ($\cdots$) $\mathcal{P}_{12}$, (- -) $-\varepsilon_{12}$, (- · -) D_{12}, (- · · -) Π_{12}, (- - · ·) G_{12}, (—) T_{12}, (+) C_{12}.

except for the pressure-strain and pressure diffusion at the wall which shows larger values in the Couette case. The outer ($y^+ > 5$) values are however the same in the two flows.

The outer peak (at $y^+ = 6$) of the pressure-strain equals the value at the wall in ZPG and APG2 cases. In the weaker APG boundary layer, APG1, the outer peak has a lower value than at the wall.

2.4. *Near-wall behavior*

There is a balance between dissipation and viscous diffusion on the wall. From the data in figures 2–6 we may also compute the dissipation rate anisotropies, $e_{ij} = \varepsilon_{ij}/\varepsilon - \frac{2}{3}\delta_{ij}$. The limiting values of these (along with the stress anisotropies $a_{ij} = R_{ij}/K - \frac{2}{3}\delta_{ij}$) are given in table 2 and compared with the predictions obtained by the algebraic dissipation rate anisotropy models of Hallbäck *et al.* (1990) and Sjögren & Johansson (2000). The agreement is quite satisfactory for both models in the Couette case, while the Hallbäck *et al.* model is in better agreement with DNS data for the ZPG boundary layer. In the Hallbäck *et al.* model e_{ij} is given by

$$e_{ij} = \left[1 + \alpha(\frac{1}{2}\mathrm{II}_a - \frac{2}{3})\right] a_{ij} - \alpha(a_{ik}a_{kj} - \frac{1}{3}\mathrm{II}_a\delta_{ij}), \quad \alpha = \frac{3}{4}, \tag{9}$$

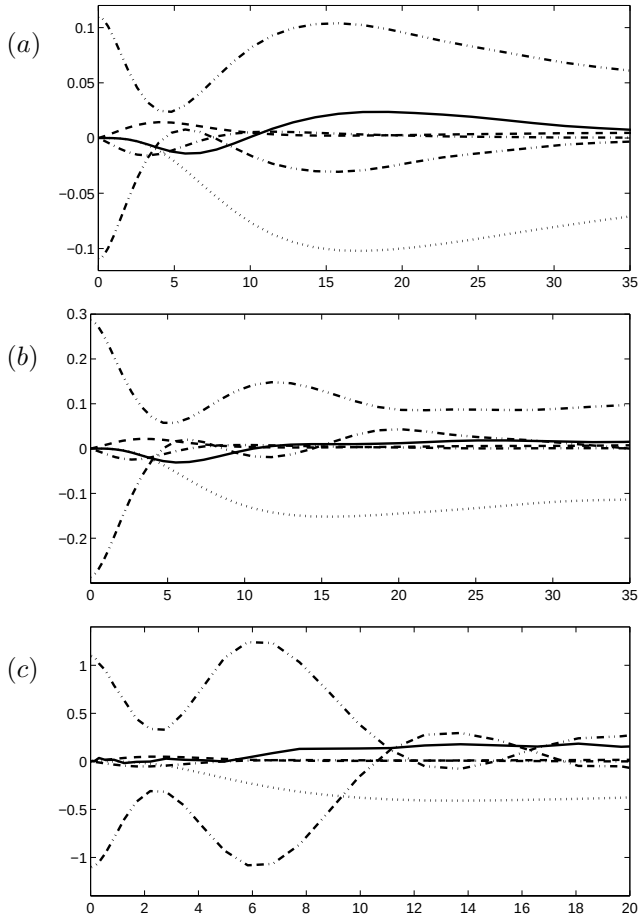

FIGURE 9. Terms in the R_{12}-budget for boundary layer flow (*a*) ZPG. (*b*) APG1. (*c*) APG2. The different terms are: $(\cdots)$ $\mathcal{P}_{12}$, (- -) $-\varepsilon_{12}$, (- · -) D_{12}, (- · · -) Π_{12}, (- - · ·) G_{12}, (—) T_{12}.

whereas in the Sjögren & Johansson model we have

$$e_{ij} = (1 - \frac{1}{2}F)a_{ij}, \quad F = 1 - \frac{9}{8}(\mathrm{II}_a - \mathrm{III}_a). \tag{10}$$

In the above expressions we have introduced the two nonzero invariants of the anisotropy tensor,

$$\mathrm{II}_a = a_{ij}a_{ji}, \tag{11}$$

$$\mathrm{III}_a = a_{ij}a_{jk}a_{ki}. \tag{12}$$

The latter model gives $e_{ij} = a_{ij}$ as limiting value in the two-component limit, such as on a solid wall. This describes the situation very accurately in both

component	1,1	2,2	3,3
a_{ij}	0.72	$-\frac{2}{3}$	-0.05
e_{ij}	0.73	$-\frac{2}{3}$	-0.06
$(e_{ij})_{\text{Hallbäck}}$	0.67	$-\frac{2}{3}$	0.00
$(e_{ij})_{\text{Sjögren}}$	0.72	$-\frac{2}{3}$	-0.05

TABLE 2. Couette data: Limiting values for the stress anisotropies a_{ij} and dissipation rate anisotropies e_{ij}, and comparison with models.

component	1,1	2,2	3,3
a_{ij}	0.76	$-\frac{2}{3}$	-0.09
e_{ij}	0.76	$-\frac{2}{3}$	-0.09
$(e_{ij})_{\text{Hallbäck}}$	0.50	$-\frac{2}{3}$	0.17
$(e_{ij})_{\text{Sjögren}}$	0.76	$-\frac{2}{3}$	-0.09

TABLE 3. Boundary layer data: Limiting values for the stress anisotropies a_{ij} and dissipation rate anisotropies e_{ij}, and comparison with models.

Case Re_{δ_*}	u^+_{rms}/y^+	$v^+_{rms}/{y^+}^2$	w^+_{rms}/y^+	$-\langle uv\rangle^+/{y^+}^3$	ε^+
ZPG 539	0.385	0.0112	0.232	0.00099	0.203
ZPG 920	0.398	0.0119	0.252	0.00102	0.223
Couette	0.414	0.0135	0.268	0.00121	0.246

TABLE 4. Limit values for $y^+ \to 0$

cases. One may note that for this extremely low Reynolds number the dissipation rate is highly anisotropic also at the centreline in the Couette case.

Some important limiting values at the wall are given in table 4 and 5. The dependence of the Reynolds number in the boundary layer is strong as seen in table 4. All the values increase for higher Reynolds number, but they do not reach the values of the Couette flow. Hence, one might argue that the Couette data constitute a high Reynolds number limit for the boundary layer.

The effect of the APG on the boundary layer is quite severe as seen from table 5. All limit values are increased when the boundary layer is subject to an APG. The rotation in the Couette case has the opposite effect; all limit values decreases.

Case	u^+_{rms}/y^+	v^+_{rms}/y^{+2}	w^+_{rms}/y^+	$-\langle uv\rangle^+/y^{+3}$	ε^+
APG1 $\beta = 0.65$	0.476	0.0177	0.344	0.00181	0.346
APG2 $\beta = 5.0$	0.728	0.0470	0.764	0.00598	1.35
Couette $\Omega = -0.005$	0.387	0.0124	0.243	0.00093	0.238

TABLE 5. Limit values for $y^+ \to 0$

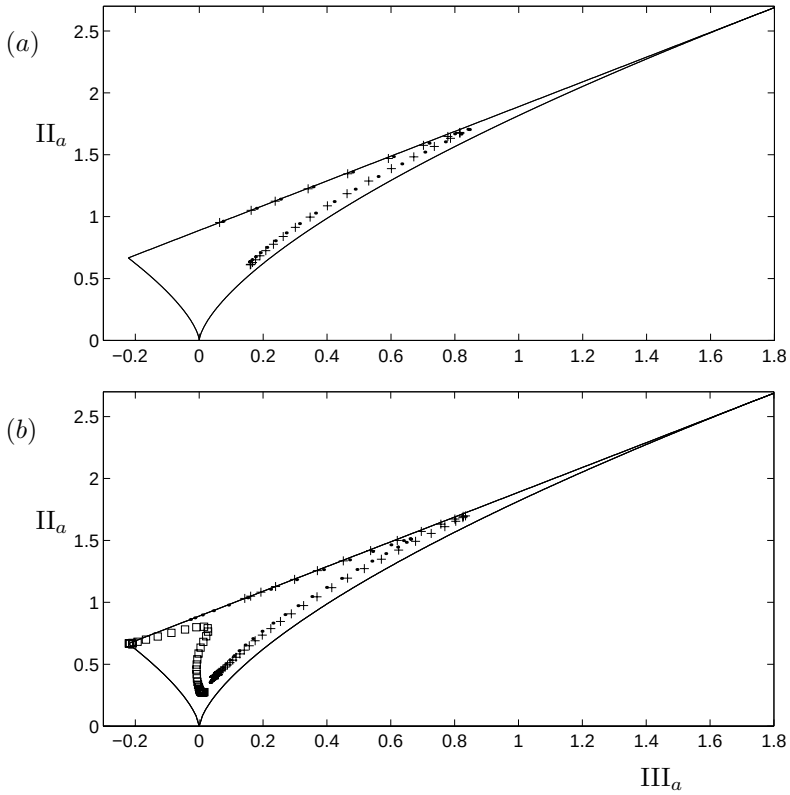

FIGURE 10. The anisotropy invariant map. a) AIM paths for the non-rotating (+) and rotating (·) case. b) AIM paths for ZPG (+) ; APG1 (·); APG2 (□).

2.5. *Anisotropy tensor*

The Reynolds stress anisotropy tensor a_{ij} has, as already mentioned above, two nonzero invariants, II_a and III_a. All anisotropic states can be represented in the anisotropy invariant map (Lumley & Newman 1977) which are bounded by the lines $8/9 + \mathrm{III}_a = \mathrm{II}_a$ and $6\mathrm{III}_a^2 = \mathrm{II}_a^3$. They represent two-component and axisymmetric turbulence, respectively.

In figure 10a the AIM paths for both the non-rotating and rotating Couette cases are shown. Their main characteristics are the same as for the channel flow simulations of Moser *et al.* (1999). Close to the wall the turbulence is very near the two-component limit, approaching the one-component limit near the edge of the viscous sublayer. At $y^+ \approx 8$ the AIM path turns towards the isotropic state. For the present cases the Re_τ is so low that there is nearly no real log-layer in the profiles with corresponding agglomeration of points in the AIM, as observed in the higher-Re channel flow simulations.

The AIM paths for the boundary layer flows are shown in figure 10b. The ZPG case is very similar to the Couette flow. There is some agglomeration of points at the end of the path which is $y^+ \approx 150$ (for ZPG). The path for APG1 starts at a lower value of III_a and represents a lower degree of anisotropy than in the ZPG case. The end of the APG1-path is at $y^+ \approx 100$. The differences between ZPG and APG1 are not so large in comparison with the APG2 case, where the path starts in the lower left corner and represents much lower degrees of anisotropy than in the other cases. This is explained by the less structured turbulence in a strong APG boundary layer. The path for APG3 was terminated at $y^+ \approx 50$, and is similar to the anisotropy states from a backward-facing step, see Le & Moin (1992).

2.6. *Pressure-strain rate split*

The results from a split of the pressure-strain rate is here presented for the Couette flow. The result from taking the divergence of the Navier–Stokes equation is a Poisson equation for the pressure,

$$\frac{\partial^2 p}{\partial x_i \partial x_i} = -\frac{\partial}{\partial x_i}\frac{\partial}{\partial x_j}(u_i' u_j') - 2\epsilon_{ijk}\Omega_j^s \frac{\partial u_k'}{\partial x_i} \tag{13}$$

with the wall boundary condition,

$$\frac{\partial p}{\partial y} = \frac{1}{Re}\frac{\partial^2 v'}{\partial y^2} - 2U\Omega^s. \tag{14}$$

By splitting the source term in the Poisson equation into one part containing the mean velocity gradient and one part containing only gradients of the fluctuating part, we may derive equations for the rapid, slow and Stokes pressure, respectively.

$$\nabla^2 p^{(\mathrm{r})} = -2\left(\frac{\partial U_i}{\partial x_k} + \epsilon_{ijk}\Omega_j^s\right)\frac{\partial u_k}{\partial x_i}, \qquad \frac{\partial p}{\partial y} = 0 \tag{15}$$

$$\nabla^2 p^{(\mathrm{s})} = -\frac{\partial u_i}{\partial x_j}\frac{\partial u_j}{\partial x_i}, \qquad \frac{\partial p}{\partial y} = 0 \tag{16}$$

$$\nabla^2 p^{(\mathrm{St})} = 0, \qquad \frac{\partial p}{\partial y} = \frac{1}{Re}\frac{\partial^2 v}{\partial y^2} - 2U\Omega^s. \tag{17}$$

The Stokes pressure is solely due to the inhomogeneous boundary condition, and may be added to either the rapid or the slow pressure. Note that the last term in the boundary condition for the Stokes pressure is non-zero only for

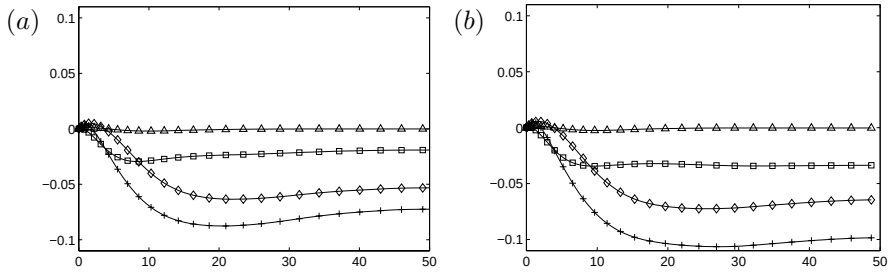

FIGURE 11. The Π_{11}-split for (a) the non-rotating case and (b) the rotating case, $\Omega = -0.005$. The different terms are: $(+)$ $\Pi_{11}^{(\mathrm{tot})}$, $(\diamond)$ $\Pi_{11}^{(\mathrm{s})}$, $(\square)$ $\Pi_{11}^{(\mathrm{r})}$, $(\triangle)$ $\Pi_{11}^{(\mathrm{St})}$.

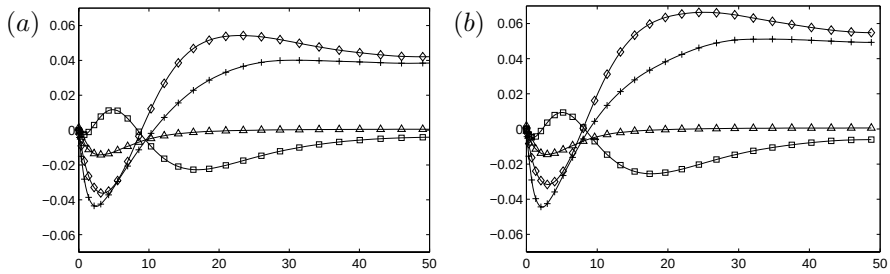

FIGURE 12. The Π_{22}-split for (a) the non-rotating case and (b) the rotating case, $\Omega = -0.005$. The different terms are: $(+)$ $\Pi_{22}^{(\mathrm{tot})}$, $(\diamond)$ $\Pi_{22}^{(\mathrm{s})}$, $(\square)$ $\Pi_{22}^{(\mathrm{r})}$, $(\triangle)$ $\Pi_{22}^{(\mathrm{St})}$.

a moving wall, e.g. Couette flow. Restricting ourself to the present case of a channel with two homogeneous directions the rapid part simplifies further,

$$\nabla^2 p^{(r)} = -2\frac{\mathrm{d}U}{\mathrm{d}y}\frac{\partial v}{\partial x} - 2\Omega^s \omega_3. \tag{18}$$

The split into rapid, slow and Stokes pressure strain-rate can be seen in figure 11–14 for Π_{11}–Π_{12}. The slow part of Π_{11} is larger than the rapid except near the wall, $y^+ < 10$, where the mean velocity gradient is large. The rapid part is more affected by the rotation than the slow part.

Also for the Π_{22}-term the slow part is larger than the rapid part, and contribute most to the pressure strain-rate. Here the slow part is more affected by the rotation.

For the Π_{33}-terms the rapid part contributes most, except for $y^+ < 10$, and is also most affected by the rotation.

The Stokes part for Π_{22}, Π_{33} and Π_{12} is significant only in the region $y^+ < 10$, and for Π_{11} it is negligible throughout the channel.

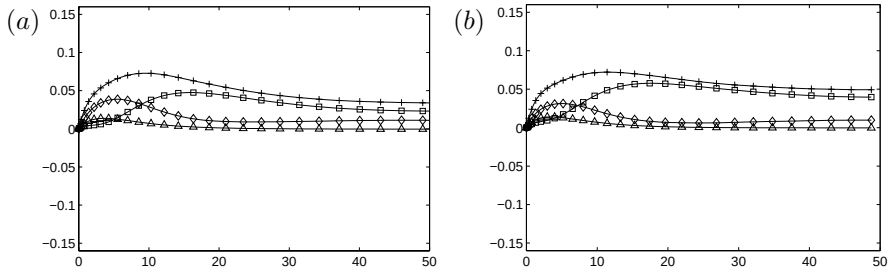

FIGURE 13. The Π_{33}-split for (a) the non-rotating case and (b) the rotating case, $\Omega = -0.005$. The different terms are: (+) $\Pi_{33}^{(\mathrm{tot})}$, ($\diamond$) $\Pi_{33}^{(\mathrm{s})}$, ($\square$) $\Pi_{33}^{(\mathrm{r})}$, ($\triangle$) $\Pi_{33}^{(\mathrm{St})}$.

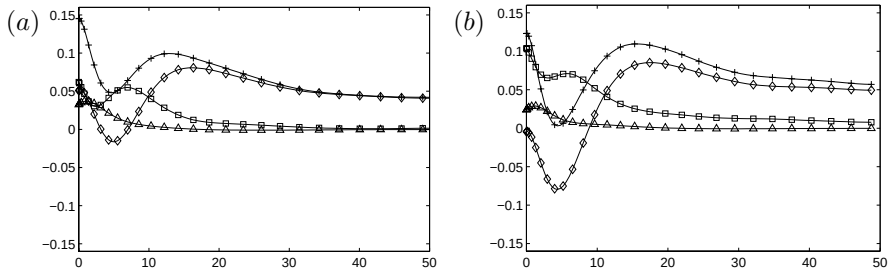

FIGURE 14. The Π_{12}-split for (a) the non-rotating case and (b) the rotating case, $\Omega = -0.005$. The different terms are: (+) $\Pi_{12}^{(\mathrm{tot})}$, ($\diamond$) $\Pi_{12}^{(\mathrm{s})}$, ($\square$) $\Pi_{12}^{(\mathrm{r})}$, ($\triangle$) $\Pi_{12}^{(\mathrm{St})}$.

The general character and amplitude of the various pressure strain rate terms are almost identical even for $Re = 375$, despite the low Reynolds number.

3. Summary

We have used the Couette flow simulation data of Komminaho *et al.* (1996) and the boundary layer data of Skote *et al.* (1998); Skote & Henningson (2000) to compute terms in the transport equation for the Reynolds stresses. For the Couette flow we have also presented data for a split of the pressure strain rate term in rapid, slow and Stokes. Data was presented for both rotating (slow stabilizing rotation) and non-rotating Couette flow. One can see a small effect of the rotation on the limiting values at the wall in the Couette flow, but it is small as could be expected, since it is a very slow rotation. In the centre of the channel the budgets were strongly influenced by the rotation.

Boundary layer data were presented for one zero pressure gradient flow and two adverse pressure gradient flows. Strong influence on the budgets from the adverse pressure gradient were detected. The near-wall limits of turbulence statistics were shown to increase with Reynolds number in the zero pressure

gradient boundary layer, but they did not reach the values obtained from the Couette flow.

Acknowledgements

The authors would like to thank Arne Johansson for many valuable comments on the manuscript.

References

Aronson, D., Johansson, A. V. & Löfdahl, L. 1997 Shear-free turbulence near a wall. *J. Fluid Mech.* **338**, 363–385.

Basdevant, C. 1983 Technical improvement for direct numerical simulation of homogeneous three-dimensional turbulence. *J. Comp. Phys.* **50** (2), 209–214.

Bech, K. H. 1995 Simulation of rotating and non-rotating turbulent plane Couette flow. PhD thesis, Department of Applied Mechanics, Thermodynamics and Fluid dynamics, Norwegian Institute of Technology, Trondheim.

Bech, K. H. & Andersson, H. I. 1994 Very-large-scale structures in DNS. In *Direct and Large-Eddy Simulations I* (eds. P. R. Voke, L. Kleiser & J.-P. Chollet), pp. 13–24. Dordrecht: Kluwer.

Bech, K. H., Tillmark, N., Alfredsson, P. H. & Andersson, H. I. 1995 An investigation of turbulent Couette flow at low Reynolds numbers. *J. Fluid Mech.* **286**, 291–325.

Ching, C. Y., Djenidi, L. & Antonia, R. A. 1995 Low-reynolds-number effects in a turbulent boundary layer. *Exps. Fluids* **19**, 61–68.

Fernholz, H. H. & Finley, P. J. 1996 The incompressible zero-pressure-gradient turbulent boundary layer: An assessment of the data. *Prog. Aerospace Sci.* **32**, 245–311.

Gibson, M. M. & Launder, B. E. 1978 Ground effects on pressure fluctuations in the atmospheric boundary layer. *J. Fluid Mech.* **86**, 491–511.

Groth, J. 1991 Description of the pressure effects in the Reynolds stress transport eqautions. *Phys. Fluids A* **3** (9), 2276–2277.

Hallbäck, M., Groth, J. & Johansson, A. V. 1990 An algebraic model for non-isotropic turbulent dissipation rate term in Reynolds stress closures. *Phys. Fluids A* **2** (10), 1859–1866.

Hunt, J. C. R. & Graham, J. M. R. 1978 Free-stream turbulence near plane boundaries. *J. Fluid Mech.* **84**, 209–235.

Kim, J., Moin, P. & Moser, R. 1987 Turbulence statistics in fully developed channel flow. *J. Fluid Mech.* **177**, 133–166.

Komminaho, J., Lundbladh, A. & Johansson, A. V. 1996 Very large structures in plane turbulent Couette flow. *J. Fluid Mech.* **320**, 259–285.

Komminaho, J., Lundbladh, A. & Johansson, A. V. 1997 Determination of the transition Reynolds number in plane couette flow through study of relaminarization. In *First AFOSR Int. Conf. on DNS/LES* (eds. C. Liu & Z. Liu), pp. 233–240. Louisiana Tech University, Ruston, LA, USA: Grayden Press.

Kreiss, H.-O. & Oliger, J. 1972 Comparison of accurate methods for the integration of hyperbolic equations. *Tellus* **24**, 199–215.

Le, H. & Moin, P. 1992 Direct numerical simulation of turbulent flow over a backward facing step. In *Annual Research Briefs*, pp. 161–173. Stanford Univ. Center for Turbulence Research.

Lumley, J. L. & Newman, G. R. 1977 The return to isotropy of homogenous turbulence. *J. Fluid Mech.* **82**, 161–178.

Lundbladh, A. & Johansson, A. V. 1991 Direct simulation of turbulent spots in plane Couette flow. *J. Fluid Mech.* **229**, 499–516.

Mansour, N. N., Kim, J. & Moin, P. 1988 Reynolds-stress and dissipation-rate budgets in a turbulent channel flow. *J. Fluid Mech.* **194**, 15–44.

Moin, P. & Kim, J. 1982 Numerical investigation of turbulent channel flow. *J. Fluid Mech.* **118**, 341–377.

Moser, R. D., Kim, J. & Mansour, N. N. 1999 Direct numerical simulation of turbulent channel flow up to $\mathrm{Re}_\tau = 590$. *Phys. Fluids* **11** (4), 943–945.

Na, Y. & Moin, P. 1996 Direct numerical simulation of studies of turbulent boundary layers with adverse pressure gradient and separation. *Tech. Rep.* TF-68. Thermosciences Division, Department of Mechanical Engineering, Stanford University.

Nagano, Y., Tagawa, M. & Tsuji, T. 1992 Effects of adverse pressure gradients on mean flows and turbulence statistics in a boundary layer. In *Turbulent Shear Flows 8* (eds. F. Durst, R. Friedrich, B. E. Launder, F. W. Schmitd, U. Schumann & J. H. Whitelaw), pp. 7–21. Springer-Verlag.

Orszag, S. A. 1969 Numerical methods for the Simulation of Turbulence. *Phys. Fluids Suppl. II* **12**, 250–257.

Orszag, S. A. 1970 Transform method for the calulation of vector-coupled sums: Application to the spectral form of the vorticity equation. *J. Athmosph. Sci.* **27**, 890–895.

Perot, J. B. & Moin, P. 1995 Shear-free turbulent boundary layers. part 1. physical insights into near-wall turbulence. *J. Fluid Mech.* **295**, 199–227.

Sahay, A. & Sreenivasan, K. 1999 The wall-normal position in pipe and channel flow at which viscous and turbulent shear stresses are equal. *Phys. Fluids* **11** (10), 3186–3188.

Sjögren, T. & Johansson, A. V. 2000 Development and calibration of algebraic nonlinear models for terms in the Reynolds stress transport equations. *Phys. Fluids* **12** (6), 1554–1572.

Skote, M., Henkes, R. A. W. M. & Henningson, D. S. 1998 Direct numerical simulation of self-similar turbulent boundary layers in adverse pressure gradients. *Flow, Turbulence and Combustion* **60**, 47–85.

Skote, M. & Henningson, D. 1999 Analysis of the data base from a dns of a separating turbulent boundary layer. Center for Turbulence Research, Annual Research Briefs 1999, 225–237.

Skote, M. & Henningson, D. S. 2000 Direct numerical simulation of a separating turbulent boundary layer. *J. Fluid Mech.* (Submitted).

Spalart, P. R. 1988 Direct simulation of a turbulent boundary layer up to $Re_\theta = 1410$. *J. Fluid Mech.* **187**, 61–98.

Spalart, P. R. & Watmuff, J. H. 1993 Experimental and numerical study of a turbulent boundary layer with pressure gradients. *J. Fluid Mech.* **249**, 337–371.

Tillmark, N. & Alfredsson, P. H. 1992 Experiments on transition in plane Couette flow. *J. Fluid Mech.* **235**, 89–102.